Engineering Bimetallic Ag-Cu Nanoalloys for Highly Efficient Oxygen Reduction Catalysts:

Wu, Xiaoqiang; Chen, Fuyi; Zhang, Nan; Qaseem, Adnan; Johnston, Roy L

DOI:
10.1002/smll.201603876

Engineering Bimetallic Ag-Cu Nanoalloys for Highly Efficient Oxygen Reduction Catalysts: A Guideline for Designing Ag-based Electrocatalysts with comparable to Pt/C-20%

Xiaoqiang Wu,[a] Fuyi Chen, [a *] Nan Zhang,[a] Adnan Qaseem [a] and Roy L. Johnston [b *]

[a]State Key Laboratory of Solidification Processing, Northwestern Polytechnical University, Xian, 710072, China

[b] Department of Chemistry, University of Birmingham, Birmingham, B15 2TT, U.K.

*Corresponding author. Tel./fax: +86029-88492052.
E-mail address: fuyichen@nwpu.edu.cn (Fuyi Chen)

Abstract: Development of highly active and stable Pt-free oxygen reduction reaction(ORR) catalysts from earth-abundant elements remains a grand challenge for highly demanded fuel cells and metal-air batteries. Ag-based alloys have many advantages over other alloy catalysts due to their low cost, high stability and acceptable ORR performance in alkaline solutions. Nevertheless, comparing to the commercial Pt/C-20%, their catalytic activity still cannot meet the demand of commercialization. Here, a kind of catalysts screening strategy on Ag_xCu_{100-x} nanoalloys is reported, containing the surface modification method, studies of activity enhancement mechanism and applied research in zinc-air batteries. These nanoalloys are first deposited on glassy carbon electrode (GDE) by laser pulse deposition(PLD), and further processed by selective dealloyed or galvanic displacement (GD). The results exhibited that the role of selective dealloying or galvanic displacement for Ag_xCu_{100-x} alloys is limited by "parting limitation" and this "parting limitation" determines the surface topography, position of d-band center and ORR performance of them. The best performing GD-$Ag_{55}Cu_{45}$ and DE-$Ag_{25}Cu_{75}$ catalysts exhibits highly ORR activity and excellent stability in 0.1M KOH, which is greatly superior to Ag and comparable to Pt/C-20%. The relationship between electronic perturbation and ORR activity demonstrated that positive shift d-band center (0.12eV) for GD-$Ag_{55}Cu_{45}$ and DE-$Ag_{25}Cu_{75}$ is benefit, which contrary to the role of electronic perturbation on Pt-based alloys (negative shift ~0.1eV). Meanwhile, extensive electrochemical and electronic structure characterization indicate the high work function of GD-$Ag_{55}Cu_{45}$ (4.9eV) would be one reason of their excellent durability for zinc-air batteries.

Key words: Ag-based alloy; oxygen reduction; electronic perturbation; d-band centre; parting limitation

1. Introduction

Aiming to engineering metal-air batteries with high specific energy and energy density, many alloy catalysts with high activity and stability have been widely studied, such as Pt-based alloys,[1-4] Pd-based alloys and Au-based alloys.[5, 6] To data, the Pt-M alloys have been known as the best catalysts for oxygen reduction reaction (ORR). Unfortunately, owing to the high cost ($1432.1 per troy oz) and low storage of Pt, their practical use have been widely impeded.[7-11] Ag-based alloys have many advantages over other alloy catalysts due to low cost (roughly 120 times cheaper than Pt) and acceptable over-potential for ORR (~50-100mV larger than Pt) in alkaline solution,[12, 13] which show enormous potential to serve as an ORR catalyst in metal-air batteries to substitute Pt-based catalysts. Nevertheless, there are still many challenges ahead, including improving the slow kinetics and low ORR active of activated Ag atoms (approximately ten times less activity than Pt atoms).[14-18]

Recently, the selective dealloying technology have emerged as a promising candidate for activity enhancement. By selective leaching the exposed less noble metals (*eg.* Co, Ni and Cu) under potential control, the dealloyed catalysts will form a incompletely noble metal shell (about three to five atomic layers deep) exposing more plentiful step surface and active site,[19] which significantly improve the activity and stability of Pt-based alloys.[3, 20-23] But for Ag-based alloys, the role of selective dealloying on ORR activity remain unclear.[24, 25] The design goal of Pt-based alloy is to decrease the adsorption energy (E_{ad}) of O-species (O, OH and OOH) to improve the ORR performance;[9-11, 26] on contrary, for Ag-based alloys, the main purpose is to improve the E_{ad} of the O-species to improve reaction kinetics and active of Ag atoms.[7, 27] Thus, the step surface, formed by selective dealloying, is good for activity enhancement for Pt-based catalysts; but for Ag-based alloys, this mechanism may have some opposite effect. Recently, an important experimental studies on dealloyed AgCo alloy present that the ORR performance of AgCo-leached (incomplete shell) is slightly worse than AgCo-heat/quenched (complete shell).[28] The density function theory (DFT) studies on dealloyed AgAl catalyst demonstrated that the step surface is not beneficial for the ORR performance.[24] Interestingly, compared to the ORR performance of original AgCo (slow reduction) and AgAl alloys, the activity and stability of dealloyed-AgCo and dealloyed-AgAl are indeed improved by selective dealloying. Hence, it's necessary to systematic study the role of selective dealloying on activity of Ag-based alloys and further understand the origin of activity enchantment by selective dealloying.

Herein, a family of dealloyed Ag_xCu_{100-x} (DE-Ag_xCu_{100-x}, x= 0, 20, 45, 50, 55, 75, 90, 100) alloys was prepared via combining the approach of pulse laser deposition (PLD) and selective dealloying method. The relationship, between initial composition and ORR activity of DE-Ag_xCu_{100-x} catalysts, exhibits that the role of selective dealloying on Ag-Cu alloys is limited by "parting limitation", and this "parting limitation" determines the surface topography, d-band center and ORR performance of DE-Ag_xCu_{100-x} alloys. Among various DE-Ag_xCu_{100-x} alloys, the DE-$Ag_{45}Cu_{55}$ catalyst exhibits best ORR performance in 0.1M KOH solution which is a more than fivefold improved performance in area-specific ORR activity compared to Initial-$Ag_{45}Cu_{55}$ at $0.8V_{RHE}$. The relationship between electronic perturbation and ORR activity demonstrated that positive shift d-band center (0.12eV) for DE-$Ag_{25}Cu_{75}$ is contrary to the role of electronic perturbation for Pt-based alloys (negative shift ~0.1eV). As a comparison, we propose a new combined design for Ag_xCu_{100-x} alloys via directly deposit Ag_xCu_{100-x} alloys on glassy carbon electrode by PLD and processing the surface of these alloys by galvanic displacement (GD-Ag_xCu_{100-x}). Compared to the DE-Ag_xCu_{100-x} alloys, the GD-$Ag_{55}Cu_{45}$ catalyst, with highest ORR performance among GD-Ag_xCu_{100-x}, exhibits higher stability than DE-$Ag_{45}Cu_{55}$ in LSV-AST test due to the higher work function(4.9eV). But for the discharge curve and ORR At last, the electrochemical activity test and line scan voltammetric accelerated stability test (LSV-AST) and durability test on Zn-air batteries suggest that the GD-$Ag_{45}Cu_{55}$ catalyst is more durability than Pt/C-20%. Our results explained the effect of electronic perturbation(come from the role of surface modification) on the activity and stability of Ag-based alloys and provide an answer as to how to further improve the ORR performance of the Ag-based catalysts.

2. Results and Discussion

2.1. Preparation of the DE- Ag_xCu_{100-x} and GD-Ag_xCu_{100-x} Catalysts

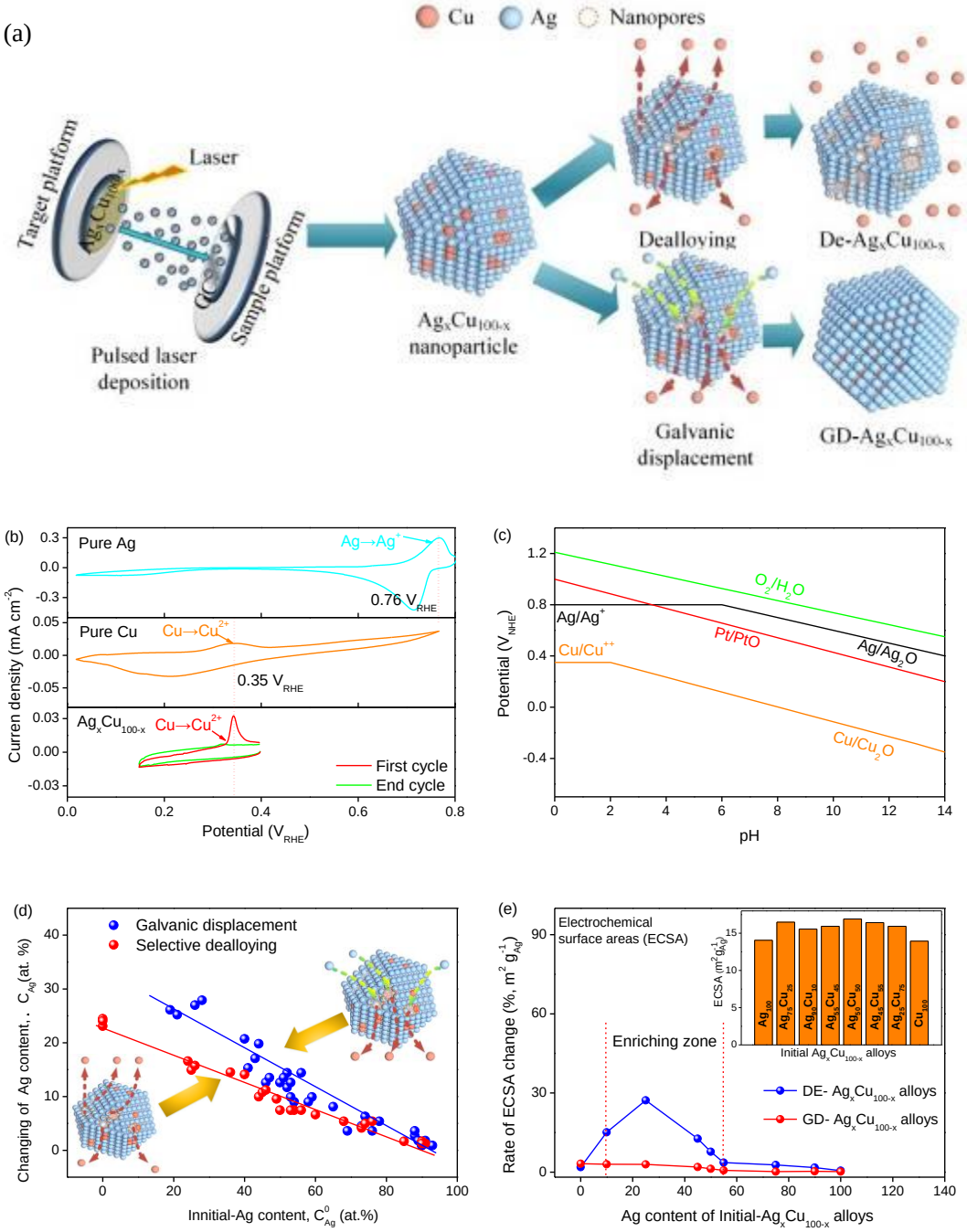

Figure 1. (a) Preparation of the DE-Ag_xCu_{100-x} and GD-Ag_xCu_{100-x} catalysts. (b) Dealloying CV curves which shows the dissolution of pure Cu, Ag and Ag_xCu_{100-x} alloys in Ar-purged 0.01M HCl + 0.1 M KCl solution. (c) Pourbaix diagram for the oxidation Ag and Cu. (d) The change of the Ag content due to selective dealloying and Galvanic displacement, characterized in a high-resolution XPS. (e) The change of the electrochemical surface area (ECSA) of De-Ag_xCu_{100-x} and Gd-Ag_xCu_{100-x} processed by selective dealloying and Galvanic displacement.

As present in **Figure1a**, unlike other forms of preparation methods, in the first step, the initial-Ag_xCu_{100-x} catalysts were directly deposited on glassy carbon electrode (GCE), with no

binder(PTFE), carbon and other impurities. Next, the initial-Ag_xCu_{100-x} catalysts were further processed by two different ways: One is selective dealloying exposed Cu from initial-Ag_xCu_{100-x} catalysts in Ar-purged 0.01M HCl + 0.1 M KCl solution with cyclic voltammetry treatment shown in **Figure 1b**. As present, the oxidation peak potentials of pure Ag ($Ag \rightarrow Ag^+$) and pure Cu($Cu \rightarrow Cu^{2+}$) are separately closed to 0.76 V_{RHE} and Cu (0.35 V_{RHE}). Thus, the applied potential of CV was precise controlled between 0.15 V_{RHE} and 0.4 V_{RHE} to selective dealloying the Cu from initial-Ag_xCu_{100-x} and preserving Ag. The CV curve of initial-Ag_xCu_{100-x} present a oxidation peak at 0.35V_{RHE} which can be index to oxidation of Cu($Cu \rightarrow Cu^{2+}$, see **Figure 1b**). This dealloying potential is coincide with the Pourbaix diagram of Ag/Ag^+ and Cu/Cu^{++}, which present similar dealloying potential of Ag(0.8V_{NHE}) and Cu(0.38V_{NHE}), as shown in **Figure 1c**.[28, 29] Second one is replace the Cu atoms on surface of initial-Ag_xCu_{100-x} catalysts by Galvanic displacement (GD) in 0.001M $AgNO_3$ solution for 3 seconds. As shown in **Figure 1a,** the exposed Cu atoms will be displaced by Ag and form new shell, more information can be seen in TEM results. Although we are aware that the concentration of $AgNO_3$ and the time of reaction for $2Ag^+ + Cu \rightarrow Cu^{2+} + 2Ag$ would influence the ORR performance of GD-Ag_xCu_{100-x} catalysts, here, we emphasize that these catalysts prepared by GD that have difference ORR performance from the DE-Ag_xCu_{100-x} catalysts. This displacement was found to be critical to achieving Ag shell on Ag_xCu_{100-x} catalysts which would significantly improve the stability and activity of initial-Ag_xCu_{100-x} in this work.

Figure 1d present the change of Ag content in DE-Ag_xCu_{100-x} and GD-Ag_xCu_{100-x} catalysts. The roughly linear relationship between initial-Ag content (C^o_{Ag}, at%) and the content change in DE-Ag_xCu_{100-x} and GD-Ag_xCu_{100-x} (ΔC_{Ag}, at%) catalysts exhibited the exposed Cu is selectively leached or displaced by Ag during surface processing. However, if the Ag content of the initial-Ag_xCu_{100-x} becomes extremely high (C^o_{Ag} >75%) , the content change was founded to be negligible in both DE- Ag_xCu_{100-x} (~1.2%) and GD-Ag_xCu_{100-x} (~1.5%) alloys. At high initial-Ag content regime(C^o_{Ag}<75%), the Ag content is greatly increased in both DE-Ag_xCu_{100-x} (~7%-~15%) and GD-Ag_xCu_{100-x} (~7%-~15%) alloys present a range as effective Ag-enriching zone due to the exposed Cu is selective dealloyed during electrochemical cycling (as equation 1) or is replaced by Ag during replacement reaction (as equation 2).

$$Cu \rightarrow Cu^{2+} + 2e^- \quad (1)$$

$$Cu + 2Ag^+ \rightarrow 2Ag + Cu^{2+} \quad (2)$$

Electrochemical surface area (ECSA) is another sensitive parameter on surface modification which directly present the situation of active sites.[30] **Figure 1e** present the evolution of ECSA measured by

Pb-stripping. Details of the Pb-stripping measurement were showed in **Experiment Section** and **Supporting Information**. As present, the ECSA of GD-Ag_xCu_{100-x} is decreased with the increasing of Ag content in initial-Ag_xCu_{100-x}. At high Ag content regime (C^o_{Ag} >75 at%), replacement reaction does not results in a obvious ECSA change (~0.2%) indicating the impact of GD is weak on the surface of catalysts. At low Ag content regime, range from 55 to 75 at %, there's an ECSA change (3% - 6%) with replacement reaction (approximately ~10 at% - ~30 at% exposed Cu replaced by Ag, see **Figure 1d**). In contrast, the ECSA of DE-Ag_xCu_{100-x} is obviously higher than GD-Ag_xCu_{100-x}; the trends of ECSA exhibited a volcano distribution and the selective dealloying procedure has good effect for the ECSA change at the 'enriching zone' (C^o_{Ag} is between 10 at% and 45 at%). However, at high initial-Ag content(C^o_{Ag}>75), selective dealloying is limited by "parting limit".[31] Anyhow, the selective dealloying process induces more ECSA change than Galvanic displacement generating a more rough surface on DE-Ag_xCu_{100-x}.

2.2. Catalytic Activity and Stability for the ORR

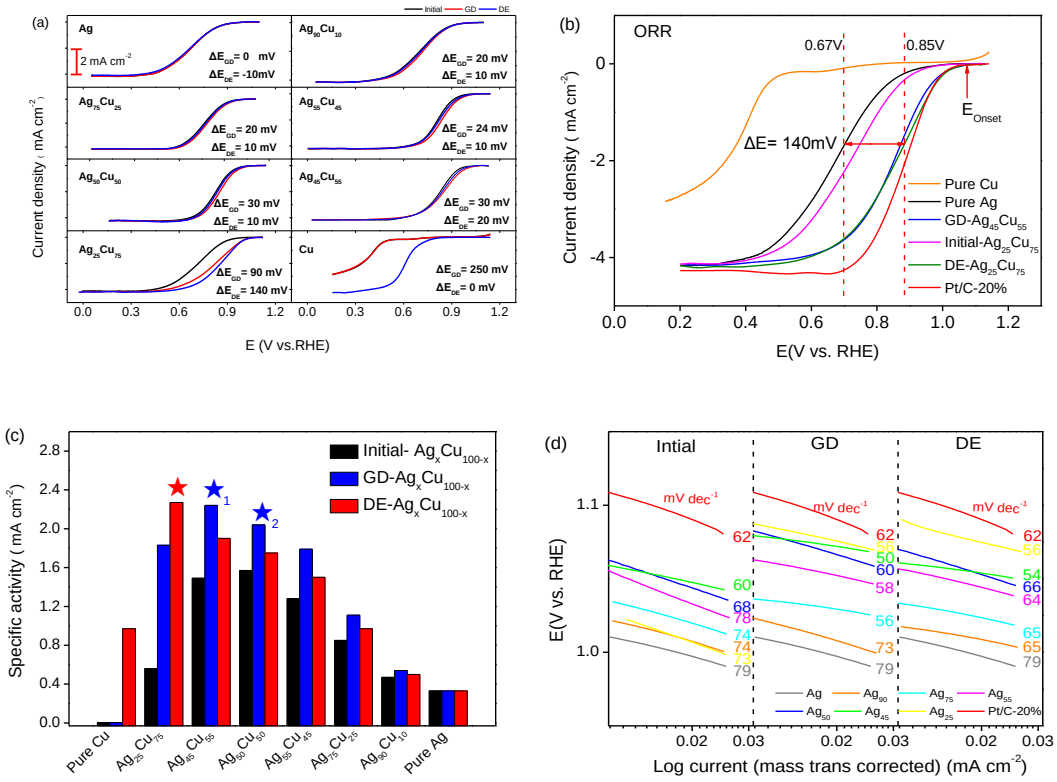

Figure 2. (a) The ORR polarization plots of initial-Ag_xCu_{100-x}, DE-Ag_xCu_{100-x} and GD-Ag_xCu_{100-x}; the Electrolyte: O_2 saturated 0.1M KOH solution, room temperature; sweep rate, 10 mV s^{-1}; rotation rate, 1600 rpm; loading is 12 μg cm^{-2}. (b) A comparison of ORR polarization plots for pure Ag, Pt/C-20%, DE-$Ag_{25}Cu_{75}$ (with best performance among DE-Ag_xCu_{100-x}) and GD-$Ag_{45}Cu_{55}$ (with best performance among GD-Ag_xCu_{100-x}). (c) Specific activity of initial-

Ag_xCu_{100-x}, DE-Ag_xCu_{100-x} and GD-Ag_xCu_{100-x} at 0.85V_{RHE}. (d) The mass-transport corrected kinetic current Tafel plots for the initial-Ag_xCu_{100-x}, DE-Ag_xCu_{100-x} and GD-Ag_xCu_{100-x} catalysts.

Table 1. The ORR activity parameters: half-wave potential (E_{half}), kinetic currents (j_{kc}), mass-corrected kinetic current (j_{mass}), electrochemical surface areas (ECSA, $m^2g^{-1}_{Ag}$) and Tafel slopes (mV dec^{-1})of the $Ag_{75}M_{25}$ and Ag_xCu_{100-x} catalysts in O_2-saturated 0.1 M KOH in positive direction at scan rate of 10 mVs^{-1} and with electrode rotation frequency of 1600 rpm.

Catalyst		Half-wave potential (V_{RHE})		Current density (mA cm^{-2})						Mass-corrected kinetic current at 0.85V_{RHE} (A g^{-1}_{Ag})		ECSA (m^2 g^{-1}_{Ag})		Tafel plots (mV dec^{-1})	
		E_{half}	ΔE_{half}	j	Δj	j_d	Δj_d	j_{kc}	Δj_{kc}	j_{mass}	Δj_{mass}	A	ΔA	K_l	ΔK_l
Initial	Pure Ag	0.67	0	0.33	0	4.15	0	0.36	0	30.0	0	14.05	0	79	0
	$Ag_{90}Cu_{10}$	0.69	0	0.47	0	4.14	0	0.53	0	44.2	0	15.52	0	74	0
	$Ag_{75}Cu_{25}$	0.76	0	0.85	0	4.19	0	1.07	0	89.5	0	16.49	0	74	0
	$Ag_{55}Cu_{45}$	0.81	0	1.28	0	4.20	0	1.85	0	154.2	0	15.93	0	78	0
	$Ag_{50}Cu_{50}$	0.82	0	1.57	0	4.21	0	2.49	0	207.5	0	16.90	0	68	0
	$Ag_{45}Cu_{55}$	0.82	0	1.49	0	4.15	0	2.33	0	194.2	0	16.43	0	60	0
	$Ag_{25}Cu_{75}$	0.71	0	0.56	0	4.13	0	0.63	0	52.5	0	15.93	0	74	0
GD	Pure Ag	0.67	0	0.33	0	4.15	0	0.36	0	30.0	0	14.08	0.03	79	0
	$Ag_{90}Cu_{10}$	0.71	0.02	0.54	0.07	4.14	0	0.62	0.90	51.7	7.5	15.56	0.04	73	-1
	$Ag_{75}Cu_{25}$	0.78	0.02	1.11	0.26	4.19	0	1.51	0.47	125.8	36.3	16.52	0.03	56	-18
	$Ag_{55}Cu_{45}$	0.83	0.02	1.79	0.51	4.21	0.01	3.11	1.26	259.2	105	16.04	0.11	58	-20
	$Ag_{50}Cu_{50}$	0.85	0.03	2.04	0.47	4.22	0.01	3.95	1.46	329.2	121.7	17.13	0.23	60	-8
	$Ag_{45}Cu_{55}$	0.85	0.03	2.24	0.75	4.16	0.01	4.86	2.53	405.0	210.8	17.59	1.16	50	-10
	$Ag_{25}Cu_{75}$	0.82	0.09	1.83	1.27	4.19	0.06	3.25	2.62	270.8	218.3	16.40	0.47	56	-18
DE	Pure Ag	0.66	-0.01	0.33	0	4.09	-0.06	0.36	0	30.0	0	14.05	0	79	0
	$Ag_{90}Cu_{10}$	0.70	0.01	0.50	0.03	4.14	0	0.57	0.04	47.5	3.3	15.78	0.26	65	-9
	$Ag_{75}Cu_{25}$	0.77	0.01	0.97	0.12	4.19	0	1.26	0.19	105	15.5	16.94	0.45	65	-9
	$Ag_{55}Cu_{45}$	0.82	0.01	1.50	0.22	4.21	0.1	2.48	0.63	206.7	52.5	16.51	0.58	64	-4
	$Ag_{50}Cu_{50}$	0.83	0.01	1.75	0.18	4.23	0.02	2.99	0.50	249.2	41.7	18.10	1.20	66	-2
	$Ag_{45}Cu_{55}$	0.84	0.02	1.90	0.41	4.18	0.03	3.49	1.16	290.8	96.6	18.52	2.09	54	-6
	$Ag_{25}Cu_{75}$	0.85	0.14	2.27	1.71	4.22	0.09	4.93	4.31	410.8	114.7	20.27	4.34	56	-18
		0.88	--	1.72	--	4.23	--	2.90	--	241.6	--	--	--	62	--

j of $Ag_{75}M_{25}$ and Ag_xCu_{100-x} catalysts is the total current density at 0.85 V_{RHE}; j of Pt/C-20% is the total current density at 0.85 V_{RHE}. j_d is the diffusion limited current density; j_{kc} is the kinetic current at 0.85V_{RHE}; j_{mass} is the mass-corrected kinetic current at 0.85V_{RHE}; K_l is the Tafel plots at low overpotentials; K_h is the Tafel plots at high overpotentials; Δ is the change of ORR performance of GD-Ag_xCu_{100-x} or DE-Ag_xCu_{100-x} alloys related to Intial-Ag_xCu_{100-x}.

We investigated the efficacy of the initial-Ag_xCu_{100-x}, DE-Ag_xCu_{100-x} and GD-Ag_xCu_{100-x} alloys for ORR at room temperature and compared it to state-of-the-art Pt/C-20%, see **Table 1** and **Figure 2**. The

summaries (see **Table 1**) of ORR polarization curves in **Figure 2a** show that all initial-Ag_xCu_{100-x} catalysts have substantially higher ORR activity than pure Ag. Moreover, comparing to the initial-Ag_xCu_{100-x} catalysts, the ORR performance of DE-Ag_xCu_{100-x} and GD-Ag_xCu_{100-x} catalysts is further improved via selective dealloying or Galvanic displacement. The selective dealloyed DE-$Ag_{75}Cu_{25}$ (real current density is 2.27 mA cm^{-2}at $0.85V_{RHE}$) and displaced GD-$Ag_{45}Cu_{55}$ (real current density is 2.24 mA cm^{-2}at $0.85V_{RHE}$) showed best ORR performance among DE-Ag_xCu_{100-x} and GD-Ag_xCu_{100-x}, respectively. This result is not surprising, because the role of parting limitation begins to weaken when the Cu content is higher than 55 at.%, the exposed Cu is easily dealloyed or displaced which will induce higher change of ECSA and Cu content(see **Figure 1d and 1e**) and further improve the ORR performance of DE-Ag_xCu_{100-x} and GD-Ag_xCu_{100-x} catalysts. As a comparing, pure Cu and DE-Cu exhibit very poor activity with a much lower limiting current than pure Ag, confirming that the enhancement of ORR performance is not contributed by pure Cu. At low Cu content regime(<50 at%), the GD-Ag_xCu_{100-x} catalysts commonly has higher ORR performance than DE-Ag_xCu_{100-x} (see **Figure 2b**). The ORR polarization plots in Figure **2c** compares the ORR performance of pure Ag, pure Cu, DE-$Ag_{75}Cu_{25}$, GD-$Ag_{45}Cu_{55}$ and Pt/C-20%, which present that the activity of DE-$Ag_{75}Cu_{25}$ and GD-$Ag_{45}Cu_{55}$ is closed to Pt/C-20%.

The kinetics of ORR were compared among the studied Initial-Ag_xCu_{100-x}, DE-Ag_xCu_{100-x}, GD-Ag_xCu_{100-x} and benchmark Pt/C-20% catalysts. Tafel slopes values for the ORR for all Ag_xCu_{100-x} catalysts are summarized in **Table 1 and Figure 2d**. For Initial-Ag_xCu_{100-x} catalysts, the Tafel slopes present a clear decreasing trend at low overpotential regime relative to pure Ag (79mV dec^{-1}), while the curves of Initial-Ag_xCu_{100-x} in **Figure 2d** present higher potential than pure Ag. After surface processing, the slopes of DE-$Ag_{25}Cu_{75}$(56 mV dec^{-1})and GD-$Ag_{45}Cu_{55}$(50 mV dec^{-1}) are further decreased relative to Initial-Ag_xCu_{100-x} suggesting an active improvement at low overpotential. It should be note here these two Tafel slops are closed to that of Pt/C-20% (62 mV dec^{-1}), indicating that the ORR mechanism of DE-$Ag_{25}Cu_{75}$ and GD-$Ag_{45}Cu_{55}$ at low overpotential is likely the same as Pt/C-20%. The GD-$Ag_{45}Cu_{55}$ present lower Tafel slopes (50 mV dec^{-1}) than DE-$Ag_{25}Cu_{75}$, despite GD-$Ag_{45}Cu_{55}$ alloys exhibit less ECSA change than DE-$Ag_{25}Cu_{75}$.

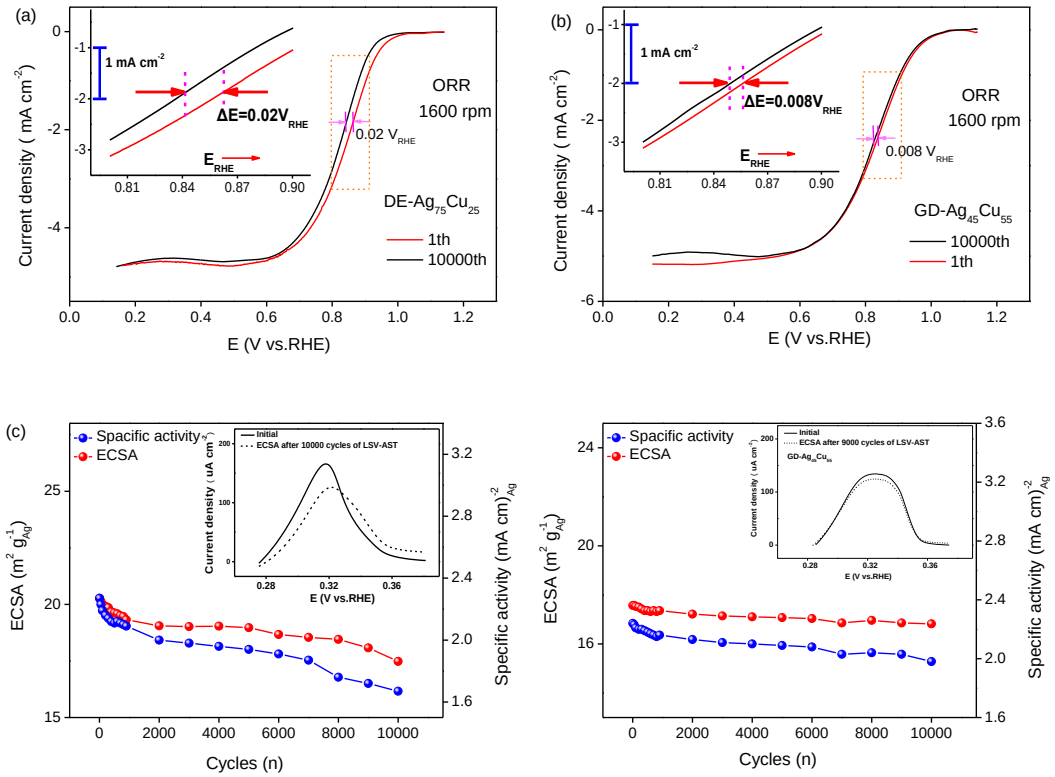

Figure 3. (a-b) A comparison of ORR polarization curves before and after 1000 cycles of line scan voltammetric accelerated stability tests (LSV-AST) for the DE-$Ag_{75}Cu_{25}$ and GD-$Ag_{45}Cu_{55}$ catalysts in O_2-saturated 0.1 M KOH; sweep rate was 10 mVs^{-1} and rotating rate was 1600 rpm. (c-d) The evolution of the corresponding electrochemical surface areas (ECSA) and specific activity (SA) of DE-$Ag_{75}Cu_{25}$ and GD-$Ag_{45}Cu_{55}$ catalysts on each stage of LSV-AST.

We also performed extensive electrochemical tests to evaluate stability of the engineered DE-$Ag_{25}Cu_{75}$ and GD-$Ag_{45}Cu_{55}$ catalysts in O_2 saturated 0.1M KOH solution over a potential window covering kinetics reaction stage (from 0.6 to 0.9V_{RHE}) at a scanning rate of 100mV s^{-1} for 10000 cycles. The stability was evaluated from the changes in half-wave potentials of the ORR polarization curves in **Figure 3a** and **3b**. As present, the DE-$Ag_{25}Cu_{75}$ catalyst exhibits exceptional stability during the long-time potential cycling test, showing only 20mV decay(from 0.86 V_{RHE} to 0.84 V_{RHE}) in half-wave potential, alone with 1.54 $m^2g^{-1}_{Ag}$ decrease in ECSA for 10000 cycles. Similarly, GD-$Ag_{45}Cu_{55}$ present just 8mV s^{-1} decay in half-wave potential, along with 0.54 $m^2g^{-1}_{Ag}$ decrease in ECSA for 10000 cycles. Combined with the trends of ECSA change and specific activity change in **Figure 3c** and **Figure 3d**, the trends provide a strong evidence that the active surface in best performing GD-$Ag_{45}Cu_{55}$ is more stable than DE-$Ag_{25}Cu_{75}$. Note that, most of DE-Ag_xCu_{100-x} studied in this work have low stability than GD-Ag_xCu_{100-x}, as present in **Table S5**. In this work, we selected the most durable and active catalysts with each of the two surface modifying methods (DE-$Ag_{25}Cu_{75}$ and GD-$Ag_{45}Cu_{55}$). They were used for

extensive structural and morphology characterization to elucidate the underlying reasons to tuning the catalytic activity and durability of these studied "bimetallic Ag_xCu_{100-x}" catalysts.

2.3. Morphology and electronic structure of Ag_xCu_{100-x} catalysts

2.3.1. Morphology on of Ag_xCu_{100-x} catalysts

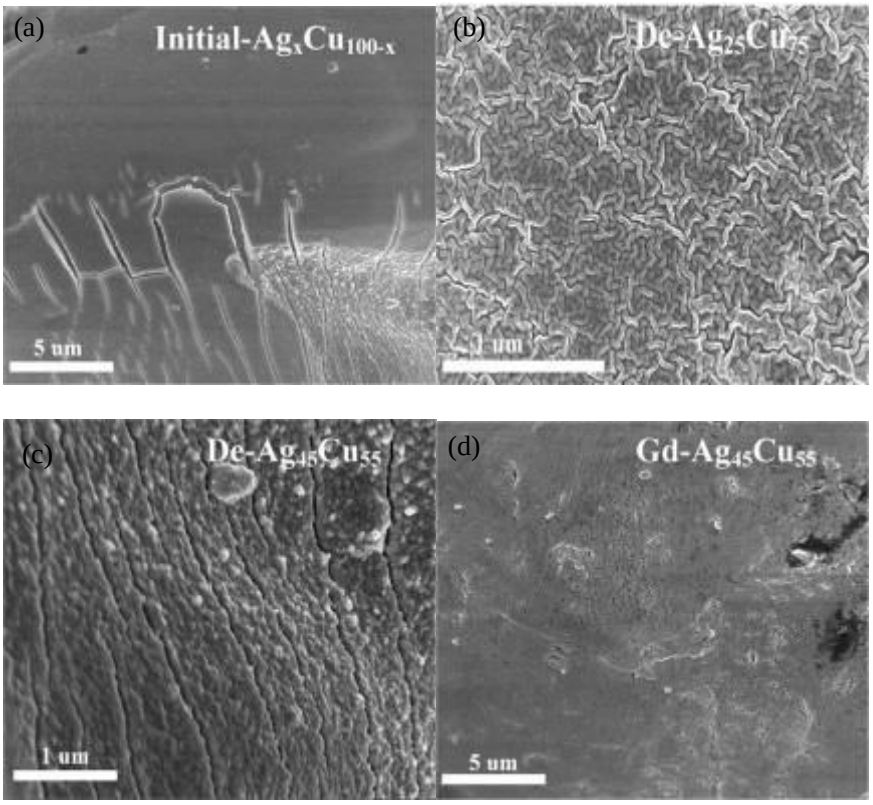

Figure 4. (a) Typical SEM image of the initial-Ag_xCu_{100-x} catalyst. (b) Microstructure of DE-$Ag_{25}Cu_{75}$ catalyst after selective dealloying. (c) Microstructure of DE-$Ag_{45}Cu_{55}$ catalyst after selective dealloying. (d) Microstructure of DE- $Ag_{45}Cu_{55}$ catalyst after Galvanic displacement.

The catalyst surface morphology plays an very important role in overall electrocatalytic activity.[1, 15, 20] Hence, to help understand the origin of the observed ORR activity and the stability enhancement, we confirmed the surface microtopography of Initial-Ag_xCu_{100-x}, GD-$Ag_{45}Cu_{55}$, DE-$Ag_{45}Cu_{55}$ and DE-$Ag_{25}Cu_{75}$ catalyst (see **Figure 4**) via field emission scanning electron microscope (FE-SEM). **Figure 4a** shows that the initial-Ag_xCu_{100-x} consisted by a film. Although the composition of Initial-Ag_xCu_{100-x} films is difference, they showed similar surface morphology under FE-SEM(see **Figure SSSS**). Here, we show a representative images of Initial-Ag_xCu_{100-x} alloys. **Figure 4b** presents the morphology of DE-$Ag_{25}Cu_{75}$ after selective dealloying. As present, the DE-$Ag_{25}Cu_{75}$ film exhibits braided strap-like morphology indicating the selective dealloying was occurred on the surface of Initial-$Ag_{25}Cu_{75}$. These

disordered and multi-gap straps exposed more surface area and facilitate access of electrolyte to the catalytically activity sites, which could be one of reasons for big ECSA change in **Figure 1e** and catalytic activity enhancement in **Figure 2**.[24] **Figure 4c** presents the images of DE-$Ag_{45}Cu_{55}$, showing some cracks on surface with no braided strap-like morphology, indicating the dealloying process is restrained with the decreasing of Cu content. Contrast to Initial-Ag_xCu_{100-x}, the GD-$Ag_{45}Cu_{55}$(see **Figure 4d**) contained a smooth surface with no obviously change in morphology.

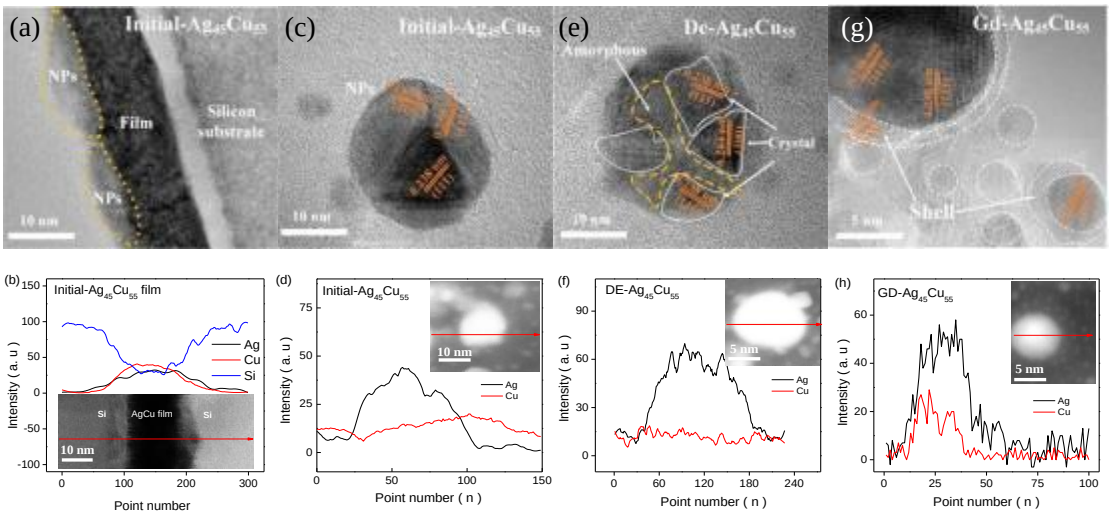

Figure 5. (a) Typical cross-sectional morphology of initial-Ag_xCu_{100-x} catalyst measured by HR-TEM image. (b) HR-TEM image of initial- $Ag_{45}Cu_{55}$ NPs. (c) HR-TEM image of DE- $Ag_{45}Cu_{55}$ NPs after selective dealloying. (d) HR-TEM image of GD- $Ag_{45}Cu_{55}$ NPs after selective dealloying. after Galvanic displacement. EDX analysis of (e) cross-sectional morphology of initial-Ag_xCu_{100-x}, (f) initial- $Ag_{45}Cu_{55}$ NPs, (g) DE- $Ag_{45}Cu_{55}$ NPs, (h) GD- $Ag_{45}Cu_{55}$ NPs

Although the change of ECSA and surface morphology of GD-$Ag_{45}Cu_{55}$ is small, the activity of GD-$Ag_{45}Cu_{55}$ is obviously enhanced compared to Initial-$Ag_{45}Cu_{55}$ (see **Figure 2**)**.** To further understand the reason of activity enhancement of GD-$Ag_{45}Cu_{55}$, we further measured the microstructure and composition of Initial-$Ag_{45}Cu_{55}$, DE-$Ag_{45}Cu_{55}$ and GD-$Ag_{45}Cu_{55}$ with high resolution transmission electron microscopy(HR-TEM) as shown in **Figure 5**. The cross-sectional morphology image (**Figure 5a**) presents that the initial- $Ag_{45}Cu_{55}$ film consists of a continuous film(basement film, ~8nm thick) and some exposing Ag-Cu nanoparticles(NPs). The particle size of NPs is ranged from 2nm to10nm. These NPs can expose more surface area and facilitate access of the electrolyte to the catalytically activity sites. **Figure 5b** presents the composition of the Initial-$Ag_{45}Cu_{55}$ film, showing the Cu and Ag are evenly distributed across all the basement film and the content of Cu (56%, atom%)is slightly higher than Ag(44%, atom %). But for NPs, the Ag content(~22 a.u.) is slightly higher than Cu(~16 a.u.). More detail information

present that the surface NPs (see **Figure 5c**) have amount clearly lattice fringes (d_l) with 0.238nm interplanar spacing, which can be index to (111) face. The results of composition analysis in **Figure 5d** further confirms that the Ag is higher than Cu in exposed NPs, which is coincide with **Figure 5b**. After dealloying, the amorphous region appeared between the crystalline regions (lattice fringes) dividing the crystalline region to three part. The crystalline regions on NPs present more various lattice fringes with 0.238 nm and 0.204 nm interplanar spacing, which can be index to (111) and (200) face. The composition analysis in **Figure 5f** present that the Cu content is decreased obviously and closed to 5% in exposed NPs, indicating the selective dealloying process is occurred on the surface of NPs(see **Figure 5e**). Although the basement film have no obviously change in surface morphology(see **Figure 4c**), the role of selective dealloying significant modified the crystal structure of exposed NPs, which could be one of reasons for their activity enhancement for ORR.

Moreover, in order to elucidate the effect of morphology on activity enhancement, we considered the morphology and composition change of the GD-$Ag_{45}Cu_{55}$ (displacement in 0.01M $AgNO_3$ for 3s, details is shown in Supporting information). When compared with the Initial-$Ag_{45}Cu_{55}$ images, the images taken after displacement showed a clear shell on the exposed NPs. Although the lattice fringes on the original NPs (d_l = 0.238nm) is in various crystal orientation, the lattice fringes of shell present the same orientation on the surface of NPs and forming a core-shell structured NPs. As present in **Equation 2**, the formation of shell can be attribute to unequal charge between Ag^+ and Cu^{++}, a Cu atom on surface of NPs can replacement two Ag ion (one filling the vacancy of Cu, the other will deposition on the surface of NPs). The composition analysis present the content of Ag is higher than Cu all over the NPs(see **Figure 5f**). The spectrum intensity of Cu (~2, a.u.) is stronger than Ag (~10, a.u.) at the edges of NPs (between 0 to 25 point number and 95 to 150 point number in curve), indicate the GD-$Ag_{45}Cu_{55}$ NPs is in core-shell structure.

2.3.2. Role of electronic perturbation on activity

Despite the DE-$Ag_{25}Cu_{75}$ and GD-$Ag_{45}Cu_{55}$ film present similar morphology on SEM images, the HR-TEM images and EDX analysis indicating the effect of morphology change on selective delloying process and Galvanic displacement is different. By galvanic displacement, the NPs on GD-$Ag_{45}Cu_{55}$ formatted more completely Ag shell on the surface and present similarly high ORR activity as DE-$Ag_{25}Cu_{75}$. Here, the exposed Ag atoms (on shell) exhibited high ORR activity. However, as prensent

in **Figure 2,** the exposed Ag atoms on pure Ag didn't present high ORR activity. Hence, there still has other issue is how the core-shell structure influence the activity of exposed pure Ag-shell. In our previous studies, we noted the role of electronic perturbation on stability and activity of Ag_xCu_{100-x} alloy nanocatalysts,[32-34] which has been demonstrated in Pt-based alloys.[9-11] The VBS of Ag would be effected by alloying with Cu on the nanometer scale. More important, the adsorption energy (E_{ad}) and dissociation energy(E_{dis}), which has been considered as the most important indexes to ORR activity, would be tuned by changing the d-band center(E_d) of VBS.[9, 11] In principle, the Cu content in Ag_xCu_{100-x} alloys may lead to two opposite roles in ORR process, one is that exposed Cu occupy active site and form a passivation coating on catalyst surface to decrease the ORR activity as activity of Cu shown in **Figure 2a**, and the other is to tune the electronic structure and modify the E_{ad} and E_{dis} of O-species (OH*,OOH* and O_2) in alkaline solution to increase the ORR performance.[35] Thus, the goal of the DE and GD surface modification methods as discussed above is to balance the Cu content in core (Cu, 45~60 at%) and the number of activity site on the surface. Then, to further understand the origin of activity enhancement on DE-$Ag_{25}Cu_{75}$ and GD-$Ag_{45}Cu_{55}$ alloys, HR-XPS was carried out to measure valence band spectrum of initial-$Ag_{45}Cu_{55}$, initial-$Ag_{25}Cu_{75}$, DE-$Ag_{25}Cu_{75}$, DE-$Ag_{45}Cu_{55}$ and GD-$Ag_{45}Cu_{55}$ alloys.

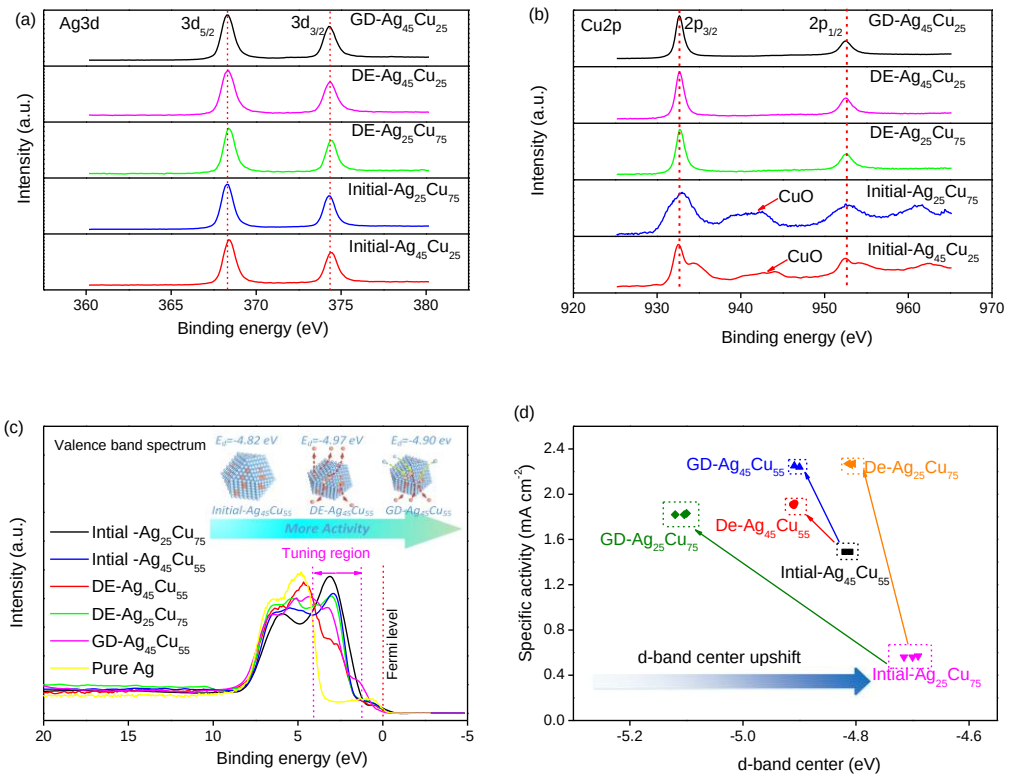

Figure 6. (a) Ag 3d regions of initial-$Ag_{45}Cu_{55}$, initial-$Ag_{25}Cu_{75}$, DE-$Ag_{25}Cu_{75}$, DE-$Ag_{45}Cu_{55}$,

GD-$Ag_{45}Cu_{55}$ and pure Ag, (b) Cu 2p regions of initial-$Ag_{45}Cu_{55}$, initial-$Ag_{25}Cu_{75}$, DE-$Ag_{25}Cu_{75}$, DE-$Ag_{45}Cu_{55}$, GD-$Ag_{45}Cu_{55}$ and pure Ag

Figure 6a and **6b** present the Ag3d and Cu2p spectrum of initial-$Ag_{45}Cu_{55}$, initial-$Ag_{25}Cu_{75}$, DE-$Ag_{25}Cu_{75}$, DE-$Ag_{45}Cu_{55}$, GD-$Ag_{45}Cu_{55}$ and pure Ag, which were fully exposed in air for 2 days before XPS measurement. The high resolution Ag3d spectra revealed two peaks of Ag, which centered at 368.27 and 374.37 eV corresponding to metallic silver (Ag^0), suggesting the silver in these alloys posses high oxidation resistance. The XPS peaks of Cu element centered at 952.47 and 932.67 eV can be assigned to Cu $2p_{3/2}$ and Cu $2p_{1/2}$ of metallic Cu (Cu^0), and the satellite peak at 942eV is from the copper oxides indicating the Cu atoms are easier oxide than Ag atoms on surface of initial-$Ag_{45}Cu_{55}$ and initial-$Ag_{25}Cu_{75}$. However, Cu 2p spectrum of the DE-$Ag_{25}Cu_{75}$, DE-$Ag_{45}Cu_{55}$ and GD-$Ag_{45}Cu_{55}$ alloys present no oxidized Cu peaks indicating that the surface Cu atoms have been cleared during selective dealloying reaction or replacement reaction and the inner Cu atoms is still in Cu^0 state.

To further understand the perturbation of inner Cu on the electronic structure, high-resolution X-ray photoelectron spectroscopy was carried out to further measure the valence band spectra (VBS) of these Ag-based alloys, details of the experiment are provided in Figure S6. The VBS spectra of the initial-$Ag_{45}Cu_{55}$, initial- $Ag_{25}Cu_{75}$, DE-$Ag_{25}Cu_{75}$, DE-$Ag_{45}Cu_{55}$, GD-$Ag_{45}Cu_{55}$ and pure Ag(see **Figure 6c**) show the surface electronic structure of Ag-Cu alloys is different from that of pure Ag, which posses a innate d-band center at -5.28eV. Careful inspection of the VBS in **Figure 6c** reveals that the density of states (DOS) of initial-$Ag_{45}Cu_{55}$, initial-$Ag_{25}Cu_{75}$, DE-$Ag_{25}Cu_{75}$, DE-$Ag_{45}Cu_{55}$, GD-$Ag_{45}Cu_{55}$ alloys present a clearly discernible increase at the tuning region (near the Fermi level, between 1eV and 3eV). Meanwhile, at the tuning region(see **Figure 6c**), the DOS of DE-$Ag_{25}Cu_{75}$,DE-$Ag_{45}Cu_{55}$ and GD-$Ag_{45}Cu_{55}$ is decreased indicate the role of electronic perturbation on DE-$Ag_{25}Cu_{75}$, DE-$Ag_{45}Cu_{55}$ and GD-$Ag_{45}Cu_{55}$ is weaker than initial-$Ag_{25}Cu_{75}$ and initial-$Ag_{45}Cu_{55}$. These results demonstrate both dealloying and

displacement process were modified the VBS of initial-$Ag_{25}Cu_{75}$ and initial-$Ag_{45}Cu_{55}$. In recent reports, the relationship between the ORR activity and d-band center of VBS have been established to guide the designs of Pt-based alloys.[9-11, 36] Here, the d-band center of VBS is adapted to address the role of electronic perturbation in Ag_xCu_{100-x} alloys and established a relationship between d-band center and the ORR activity as shown in **Figure 6d**. As present, all the d-band centers of the DE-$Ag_{25}Cu_{75}$, DE-$Ag_{45}Cu_{55}$ and GD-$Ag_{45}Cu_{55}$ alloys were downshifted relative to Initial-$Ag_{25}Cu_{75}$ and Initial-$Ag_{45}Cu_{55}$ alloys. Nevertheless, after surface modifying, their ORR activity is enhanced with the downshifting of d-band centre. This result indicating these surface modification methods changed the surface composition and microstructure of Ag_xCu_{100-x} alloys which downshifted the d-band center position and resulting in an ORR enhancement in alkaline solution. Moreover, considering the change of morphology structures in **Figure 4** and **Figure 5**, this relationship also demonstrated that the activity enhancement of GD-$Ag_{45}Cu_{55}$ and DE-$Ag_{25}Cu_{75}$ is the result of coordinated actions of electronic perturbation and morphology structures.

2.3.3. Role of electronic perturbation on stability

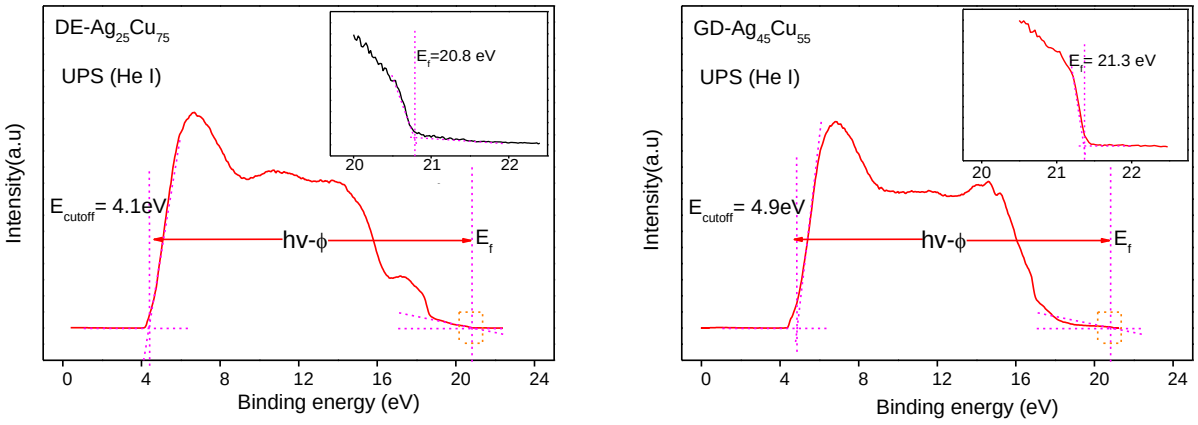

Figure 7. (a) Ultraviolet photoelectron spectroscopy (UPS) spectra of DE-$Ag_{25}Cu_{75}$ and corresponding E_{cutoff} and E_f states. (b) UPS spectra of GD-$Ag_{45}Cu_{55}$ and corresponding E_{cutoff} and E_f states.

To further understand the origin of superior stability of GD-$Ag_{45}Cu_{55}$, we measured the work

function (φ) of electron on the surface of GD-$Ag_{45}Cu_{55}$ and DE-$Ag_{25}Cu_{75}$ alloys, which is necessary to understand the influence of electronic perturbation on Ag based catalyst's stability; however, there are numerous unresolved questions and a lot of influences, as the influence of the substrate, surface morphology, interfacial effect, etc. But, as a trend, the work function (φ) is one of relevant to capture electron, which influence the corrosion resistant capacity of alloys.[37, 38] In particularly, the dissolution of metals is believed to be responsible for deactivation of binary Ag or Pt alloy catalysts and the corrosion resistant is directly related to stable of metals in alkaline solution. Here, the ultraviolet photoelectron spectroscopy (UPS) measurement were conducted to estimate the work function. The φ is determined from the following equation:[39]

$$\varphi = h_v + E_{cutoff} - E_f \quad (1)$$

where φ is work function, h_v is the energy of the UV photon (21.2eV), E_{cutoff} is the energy of the final state, E_f is the Fermi energy or the energy of the initial state. As shown in **Figure 7a** and **7b** the energy of the initial state of GD-$Ag_{45}Cu_{55}$ and DE-$Ag_{25}Cu_{75}$ is located at 20.8eV and 21.3eV , respectively; but for the energy of the final state, the E_{cutoff} of GD-$Ag_{45}Cu_{55}$ (4.9eV) is higher than DE-$Ag_{25}Cu_{75}$ (4.1eV), which result in difference work function as 4.8eV and 4.5eV, respectively. This results suggesting the completely-shell structured GD-$Ag_{45}Cu_{55}$ alloy has higher work function and more efficient to maintain the surface electron, which is effectively prevent the exposing metals(Ag) from being corrosion and enhance the catalytic stability of GD-$Ag_{45}Cu_{55}$ alloy in alkaline solution.

2.3.4. Performance of the batteries

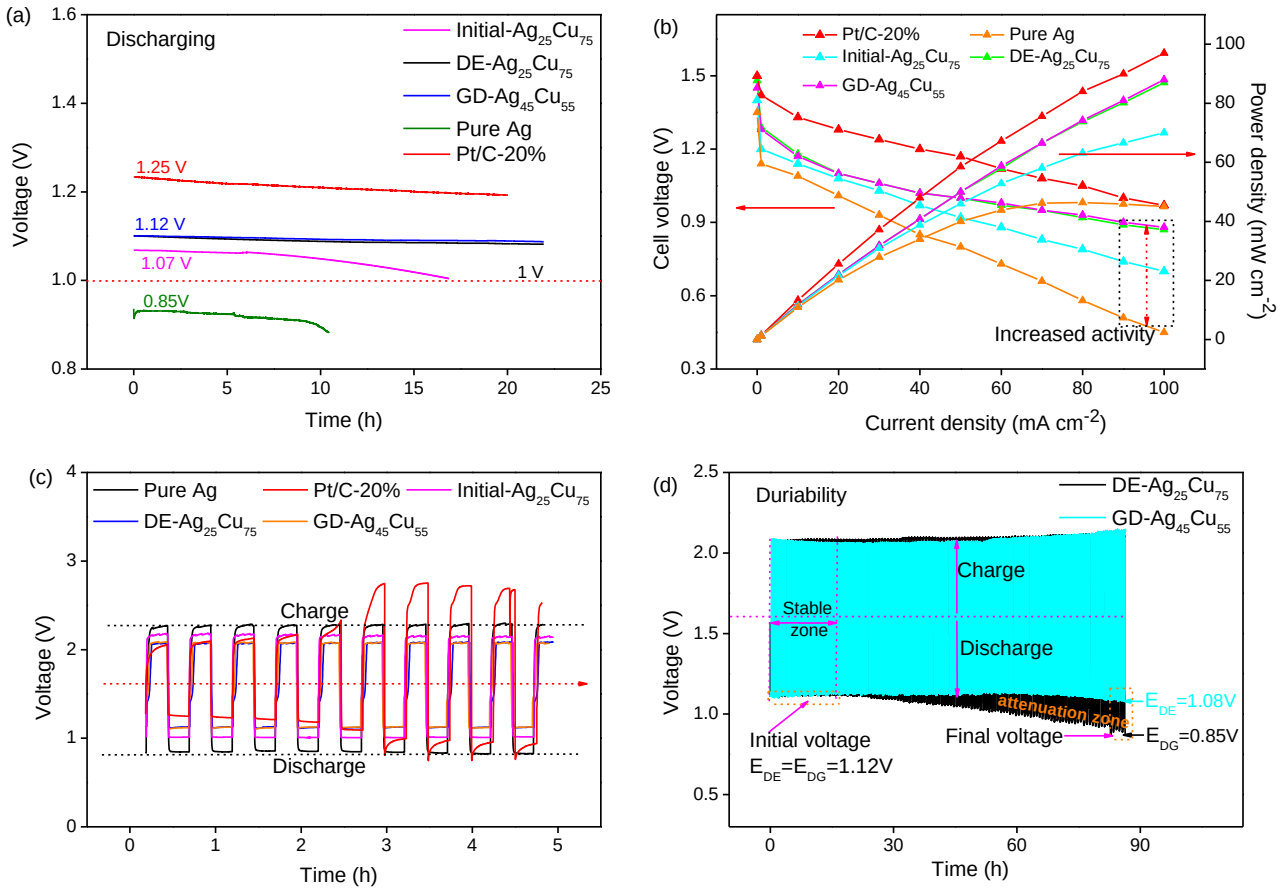

Figure 8. (a) The discharge polarization and power density curves for pure Ag, Initial-$Ag_{25}Cu_{75}$, DE-$Ag_{25}Cu_{75}$, GD-$Ag_{45}Cu_{55}$, and Pt/C-20% based catalyst layers of the primary zinc-air battery. (b) The galvanostatic discharge curves of the primary zinc-air battery at 20 mA cm^{-2} for pure Ag, Initial-$Ag_{25}Cu_{75}$, DE-$Ag_{25}Cu_{75}$, GD-$Ag_{45}Cu_{55}$, and Pt/C-20% catalysts. (c) The charge-discharge polarization curves of the pure Ag, Initial-$Ag_{25}Cu_{75}$, DE-$Ag_{25}Cu_{75}$, GD-$Ag_{45}Cu_{55}$, and Pt/C-20% based rechargeable zinc-air battery. (d) long-term cycle of rechargeable Zinc-air battery.

To further study the activity and stability of DE-$Ag_{25}Cu_{75}$ and GD-$Ag_{45}Cu_{55}$ catalysts in real battery operation conditions, a primary zinc-air battery was constructed, as shown in **Figure S6**. The galvanostatic discharge curves in **Figure 8a** exhibited a higher discharge voltage(1.07V) than pure Ag based battery (0.85V) at discharge current of 20 mA cm^{-2}, indicating that the performance of initial-$Ag_{25}Cu_{75}$ based battery is better than pure Ag based battery. Further more, the DE-$Ag_{25}Cu_{75}$ based and GD-$Ag_{45}Cu_{55}$ based batteries illustrate an discharge voltage of 1.12V with a high durability for 20 hours discharging at 20 mA cm^{-2} (discharge voltage attenuated ~ 0.005V), which further improved the discharge performance of intial-$Ag_{25}Cu_{75}$ based batteries. More important,

contrast with the performances of the commercial Pt/C-20% (loading is 1.2 mg cm^{-2}), this discharge performance (1.12V at 20 mA cm^{-2}) of DE-$Ag_{25}Cu_{75}$ and GD-$Ag_{45}Cu_{55}$ based batteries is comparable to present Pt/C–20% based batteries (1.12V at 20 mA cm^{-2}). It is noteworthy that the loading of Ag_xCu_{100-x} used in this work is only 0.012 mg cm^{-2}, which is much lower than that of Pt/C-20% system. As present in **Figure 8b**, the discharging polarization curves of DE-$Ag_{25}Cu_{75}$ and GD-$Ag_{45}Cu_{55}$based batteries exhibited a high current density of 50.12 mA cm^{-2} at 1.0V and a power density of 88 mW cm^{-2} with 100 mA cm^{-2} discharging.

The stability of the DE-$Ag_{25}Cu_{75}$ and GD-$Ag_{45}Cu_{55}$ catalysts were also investigated in rechargeable zinc-air batteries using the same construction except for adding 0.1M zinc acetate to 6M KOH electrolyte, where zinc acetate is benefited for reduce the concentration polarization in reversible recharging process. As present, the long-term charge–discharge cycling tests using a constant current density of 20 $mAcm^{-2}$, the DE-$Ag_{25}Cu_{75}$ and GD-$Ag_{45}Cu_{55}$ based batteries show higher round-trip efficiency (negligible voltage change at the end) and the smallest sum of over-potential (difference of the charge voltage and discharge voltage; 0.80V). when compared with Pt/C-20% cathodes, as shown in **Figure 8c**, the Pt/C-20% cathode presents almost the same discharge voltage of 1.23V at 20 mA cm^{-2} during the first four cycles, but after 5 cycle the discharge voltage of Pt/C-20% begin to decrease and fall off rapidly following the increasing of cycles. This result indicating DE-$Ag_{25}Cu_{75}$ and GD-$Ag_{45}Cu_{55}$ catalysts is more suitable for recharge battery than Pt/C-20%. To further comparing the stability of DE-$Ag_{25}Cu_{75}$ and GD-$Ag_{45}Cu_{55}$ catalysts we considered the long term cycle stability of them as shown in **Figure 8d**. As present, at the stable zone (initial 20h), both the catalyst based batteries have the same discharge voltage(1.12V)and have no obvious discharge voltage attenuate. After 20 hours cycle, the

discharge voltage of DE-$Ag_{25}Cu_{75}$ begin to decrease and approach to 0.85V at the end. But for, GD-$Ag_{45}Cu_{55}$ catalyst, there is no clearly decreasing of discharge voltage which maintained at 1.08 (decreased 0.04V) after 85 hours cycle. It is clear that the GD-$Ag_{45}Cu_{55}$ catalyst is more durable than DE-$Ag_{25}Cu_{75}$ during the discharging and charging processes. This result is coincide with results of LSV-AST results and confirm the Galvanic displacement method is more suitable for tune the activity and stability of the Ag-Cu alloys.

3. Conclusions

In conclusion, we prepared porous surface DE-Ag_xCu_{100-x} catalysts and core-shell structured GD-Ag_xCu_{100-x} catalysts by combined pulsed laser deposition and dealloying/galvanic displacement method respectively. Through comparing the surface composition, microtopography, valence band and work functions of DE-Ag_xCu_{100-x} and GD-Ag_xCu_{100-x} catalysts, we demonstrate that the enhancement mechanism of activity and stability have some different from Pt-based alloys; such as, in low Cu content region, the impact dealloying on active enhancement is limited by "parting limit", the positive shift d-band center (~0.18eV, relative to pure Ag) is benefit for ORR enhancement and the core-shell strcutured GD-$Ag_{45}Cu_{55}$ catalysts has higher work function(4.8eV) than DE-$Ag_{25}Cu_{75}$ which would be one reason of the high stability of GD-$Ag_{45}Cu_{55}$ catalysts. We show that the DE-$Ag_{25}Cu_{75}$ and GD-$Ag_{45}Cu_{55}$ can serve as an ideal catalysts with comparable specific activity(~2.24mA cm^{-2}) in ORR polarization test, high activity(1.17V at 20mA cm^{-2}) and excellent stability in primary zinc-air batteries. For rechargeable batteries, the stability of GD-$Ag_{45}Cu_{55}$ is far beyond the Pt/C-20%. This study systemically studied the ORR activity and stability of initial- Ag_xCu_{100-x}, GD-Ag_xCu_{100-x} and DE-Ag_xCu_{100-x} catalysts and applied them to primary and recharge Zn-air batteries which establish a guideline for the designation of Ag-based

alloys. We believe that there are numerous problems need to solve for Ag_xCu_{100-x} alloys, the way of catalyst design demonstrated in this work can be further extend for other Ag-based alloys to tune the ORR activity and durability.

4. Experiment Section

Initial-Ag_xCu_{100-x} catalysts: Initial-Ag_xCu_{100-x} catalysts were fabricated using a pulsed laser deposition (PLD) technology for all the samples. The Ag_xCu_{100-x} alloys (x=0, 25, 45, 50, 55, 75, 90 and 100) were used as sputtering target materials and fixed on an adjustable rotation rate target platform (ARRTP) of the PLD. The rotational velocity of ARRTP is maintained at 5 rpm. The glassy carbon (GC) electrode was polished in Al_2O_3 powder, cleaned in dilute sulphuric acid for 5min. After washing by deionized water in ultrasonic washer and drying in vacuum drying oven, the pre-processed GC was directly used as a substrate setting on an adjustable rotation rate sample platform (ARRSP) of the PLD and rotated at the speed of 5 rpm. The distance of the ARRSP -to- ARRTP is 10cm. The vacuum degree of sputtering cavity were first maintained at 2.0×10^{-4} Pa before sputtering and cooled by flowing helium during the deposition process. The impurity (such as copper oxide and silver oxide) on surface were first cleaned under 2Hz irradiate for 5min by YAG laser beam(wavelength: 266 nm, pulse duration: 3-6 ns, beam diameter : 1 mm, energy density: 200 mJ/pulse, EKSPLA, Lithuania). After this pre-process, all the target alloys were allowed to deposition on GC at 10Hz. All the samples were deposited with 6000 laser pulses(about 10 nm thick, 12ug/cm^{-2}). All initial-Ag_xCu_{100-x} catalysts were directly deposited on GC with no binder, carbon and other impurities, which contribute to the accuracy of the test result.

DE-Ag_xCu_{100-x} catalysts: Dealloyed Ag_xCu_{100-x} catalysts were fabricated using a selective leaching process for all the initial-Ag_xCu_{100-x} catalysts. The selective leaching procedure was carried out in argon saturated 0.01M HCl+0.1M KCl solution using cyclic votammetry at a sweep of 10mV s^{-1} between

$0.08V_{RHE}$ and $0.7V_{RHE}$. The scanning potential range(between $0.08V_{RHE}$ and $0.7V_{RHE}$) is determined by the Pourbaix diagram and the leaching diagram of pure Ag and pure Cu in prepared solution as shown in Figure 1. After selective leaching procedure, all samples were soaking in deionized (DI) water for 5 min with rotating speed of 1600 rpm.

GD-Ag_xCu_{100-x} catalysts: The galvanic displacement reaction with Ag was carried out in Ar-purged 0.001M $AgNO_3$+0.1M $NaNO_3$ for 8 seconds with out application of voltage. After displacement, all GC electrodes were soaked in 0.1M HCl for 2 min to eliminate the impurities and washed with DI water for 5min with rotating speed of 1600 rpm.

Preparation of Zn-battery: First, gas diffusion layer (GDL) is prepared by 1g of acetylene black, 5ml of PTFE (65%). The acetylene black and PTFE were first mix with 30 ml absolute ethanol and 10ml deionized water and stirred for 3 hours to form a colloidal solution. And then, separating this colloidal in ultrasonic for 15min and bath heating in 80℃ water for 10 minutes to prepare the acetylene black colloid. This acetylene black colloid was drying in vacuum drying oven and press at 10 MPa pressures for 30 minutes to prepare the GDL(~0.4mm thick). The catalyst layer (CL) were directly deposition on nickel foam as preparation of initial-Ag_xCu_{100-x} catalysts , which ensured the air permeability of air electrode. Then, fix this prepared GDL on the surface of CL and rolled them to 0.5mm and heated on a hot plate for 5 min. Finally, the electrode was cut to size for Zn-air battery. The anode is pure Zn plate (99.99%). In primary Zn-air battery, the electrolyte is 6M KOH. For rechargeable Zn-air battery, the electrolyte is 6M KOH+ $Zn(CH_3COO)_2$ solution. Here, the $Zn(CH_3COO)_2$ is conducive to lower the concentration polarization during charging process.

Microstructural Characterization: Physical characterization of pristine and surface modified Ag_xCu_{100-x} catalysts (initial-Ag_xCu_{100-x}, GD-Ag_xCu_{100-x} and DE-Ag_xCu_{100-x}) were conducted using

X-ray photoelectron spectroscopy (XPS) measurements on an ULTRA (ESCALAB 250, Al Kα, ultrahigh vacuum is 10^{-9}, hν = 1486.6 eV, No charge compensation was necessary, the origin of the binding energy E_b was set to the Fermi energy E_f of the Au plate), X-ray diffraction (XRD), high-resolution transmission electron microscopy (TEM, FEI Tecnai F30, 200 kV) analysis, scanning electron microscope (SEM) and quantitative energy dispersive spectroscopy (EDS). The d-band center of the valence band (VBS) is given by $\int R(\varepsilon)\varepsilon d\varepsilon / \int R(\varepsilon) d\varepsilon$, in this work, the R(ε) is the XPS-intensity (DOS-intensity) after background subtraction.[9]

Electrochemical testing: All electrochemical measurements were carried out by a classic three electrode set-up. The mercuric oxide electrode (Hg/HgO) was used as a reference electrode, a Pt wire electrode was employed as a counter electrode and the working electrode was fabricated by directly deposition initial-Ag_xCu_{100-x}, GD-Ag_xCu_{100-x} and DE-Ag_xCu_{100-x} catalysts layers GC as mentioned above. The linear voltammetry scanning (LSV), cyclic voltammetry(CV) and polarization curves were studied at room temperature in 0.1M KOH(O_2 saturated) on rotating disk electrode (RDE) and CHI660C electrochemical workstation. We considered IR-dropping in all of the tests. All potentials are reported relative to the Reversible Hydrogen Electrode ($V_{RHE} = V_{NHE} + 0.0591pH$).[28] The experiments were performed at a scanning rate of 10 mV s^{-1} and the rotation rates were controlled at 400, 900, 1600 and 2500 rpm.

Pb-stripping voltammetry was performed immediately after ORR measurements in 0.1M KOH+0.01M $Pb(NO_3)_2$ solution. Before Pb-stripping voltammetry test, the solution was purged with Ar for 30 minutes. The stable voltammograms were integrated assuming 280uC/cm^2, which was established based on Ag faces.[40] In this experiment, the Hg/HgO electrode was in contact with 0.1M KOH+0.01M $Pb(NO_3)_2$ solution via salt bridge, whose solution is saturated KNO_3.

The performances of the zinc-air batteries were measured and recorded by a TC 5X battery testing system (Neware Company, Shenzhen) at atmosphere in the air. Battery testing and cycling experiments were performed at 25℃ at 1 atmosphere.

1 V. R. Stamenkovic, B. Fowler, B. S. Mun, G. Wang, P. N. Ross, C. A. Lucas and N. M. Markovic, *Science*, 2007, **315**, 493-497.

2 T. Toda, H. Igarashi, H. Uchida and M. Watanabe, *Journal Of the Electrochemical Society*, 1999, **146**, 3750-3756.

3 D. L. Wang, Y. C. Yu, J. Zhu, S. F. Liu, D. A. Muller and H. D. Abruna, *Nano letters*, 2015, **15**, 1343-1348.

4 H. M. Duan, Q. Hao and C. X. Xu, *Journal Of Power Sources*, 2015, **280**, 483-490.

5 N. N. Kariuki, X. Wang, J. R. Mawdsley, M. S. Ferrandon, S. G. Niyogi, J. T. Vaughey and D. J. Myers, *Chemistry of Materials*, 2010, **22**, 4144-4152.

6 M. H. Naveen, N. G. Gurudatt, H. B. Noh and Y. B. Shim, *Adv Funct Mater*, 2016, **26**, 1590-1601.

7 K. Shin, D. H. Kim, S. C. Yeo and H. M. Lee, *Catalysis Today*, 2012, **185**, 94-98.

8 X. Y. Lang, G. F. Han, B. B. Xiao, L. Gu, Z. Z. Yang, Z. Wen, Y. F. Zhu, M. Zhao, J. C. Li and Q. Jiang, *Adv Funct Mater*, 2015, **25**, 230-237.

9 S. J. Hwang, S. K. Kim, J. G. Lee, S. C. Lee, J. H. Jang, P. Kim, T. H. Lim, Y. E. Sung and S. J. Yoo, *Journal of the American Chemical Society*, 2012, **134**, 19508-19511.

10 V. R. Stamenkovic, B. S. Mun, M. Arenz, K. J. Mayrhofer, C. A. Lucas, G. Wang, P. N. Ross and N. M. Markovic, *Nature materials*, 2007, **6**, 241-247.

11 V. Stamenkovic, B. S. Mun, K. J. J. Mayrhofer, P. N. Ross, N. M. Markovic, J. Rossmeisl, J. Greeley and J. K. Norskov, *Angew Chem Int Edit*, 2006, **45**, 2897-2901.

12 J. S. Spendelow and A. Wieckowski, *Physical Chemistry Chemical Physics*, 2007, **9**, 2654-2675.

13 Y. Li and H. Dai, *Chemical Society reviews*, 2014, **43**, 5257-5275.

14 M. Chatenet, L. Genies-Bultel, M. Aurousseau, R. Durand and F. Andolfatto, *Journal Of Applied Electrochemistry*, 2002, **32**, 1131-1140.

15 B. B. Blizanac, P. N. Ross and N. M. Markovic, *J Phys Chem B*, 2006, **110**, 4735-4741.

16 C. Coutanceau, L. Demarconnay, C. Lamy and J. M. Leger, *Journal Of Power Sources*, 2006, **156**, 14-19.

17 G. K. H. Wiberg, K. J. J. Mayrhofer and M. Arenz, *Fuel Cells*, 2010, **10**, 575-581.

18 P. Singh and D. A. Buttry, *J Phys Chem C*, 2012, **116**, 10656-10663.

19 P. Mani, R. Srivastava and P. Strasser, *J Phys Chem C*, 2008, **112**, 2770-2778.

20 C. Baldizzone, L. Gan, N. Hodnik, G. P. Keeley, A. Kostka, M. Heggen, P. Strasser and K. J. J. Mayrhofer, *Acs Catalysis*, 2015, **5**, 5000-5007.

21 C. Xu, H. Zhang, Q. Hao and H. Duan, *ChemPlusChem*, 2014, **79**, 107-113.

22 R. Yang, J. Leisch, P. Strasser and M. F. Toney, *Chemistry of Materials*, 2010, **22**, 4712-4720.

23 R. Kraehnert, E. Ortel, B. Paul, B. Eckhardt, M. Kanis, R. Liu and A. Antoniou, *Catal Sci Technol*, 2015, **5**, 206-216.

24 Y. Zhou, Q. Lu, Z. B. Zhuang, G. S. Hutchings, S. Kattel, Y. S. Yan, J. G. G. Chen, J. Q. Xiao and F. Jiao, *Advanced Energy Materials*, 2015, **5**.

25 A. Qaseem, F. Chen, X. Wu and R. L. Johnston, *Catal Sci Technol*, 2016.

26 J. Zhang, M. B. Vukmirovic, K. Sasaki, A. U. Nilekar, M. Mavrikakis and R. R. Adzic, *Journal of the American Chemical Society*, 2005, **127**, 12480-12481.

27 X. Q. Wu, F. Y. Chen, Y. C. Jin, N. Zhang and R. L. Johnston, *ACS applied materials & interfaces*, 2015, **7**, 17782-17791.

28 A. Holewinski, J. C. Idrobo and S. Linic, *Nature chemistry*, 2014, **6**, 828-834.

29 *Anti-Corros*, 1967, **14**, 28-&.

30 G. Doubek, R. C. Sekol, J. Y. Li, W. H. Ryu, F. S. Gittleson, S. Nejati, E. Moy, C. Reid, M. Carmo, M. Linardi, P. Bordeenithikasem, E. Kinser, Y. H. Liu, X. Tong, C. O. Osuji, J. Schroers, S. Mukherjee and A. D. Taylor, *Advanced materials*, 2016,

28, 1940-+.

31 Q. Chen and K. Sieradzki, *Nature materials*, 2013, **12**, 1102-1106.

32 W. Ma and F. Chen, *Theoretical Chemistry Accounts*, 2012, **132**.

33 W. Ma, F. Chen, N. Zhang and X. Wu, *Journal of molecular modeling*, 2014, **20**, 2454.

34 N. Zhang, F. Y. Chen and X. Q. Wu, *Sci Rep-Uk*, 2015, **5**.

35 K. Shin, H. Kim da and H. M. Lee, *ChemSusChem*, 2013, **6**, 1044-1049.

36 S. Jong Yoo, S. K. Kim, T. Y. Jeon, S. Jun Hwang, J. G. Lee, S. C. Lee, K. S. Lee, Y. H. Cho, Y. E. Sung and T. H. Lim, *Chemical communications*, 2011, **47**, 11414-11416.

37 J. Wang and S. Q. Wang, *Surface Science*, 2014, **630**, 216-224.

38 M. F. Juarez and E. Santos, *J Phys Chem C*, 2013, **117**, 4606-4618.

39 J. W. Niemantsverdriet, *Spectroscopy in catalysis* Wiley-VCH ;
John Wiley, distributor, Weinheim
Chichester, 2007.

40 E. Kirowa-Eisner, D. Tzur and E. Gileadi, *Journal Of Electroanalytical Chemistry*, 2008, **621**, 146-158.